


Article

Polypyrrole-Coated Low-Crystallinity Iron Oxide Grown on Carbon Cloth Enabling Enhanced Electrochemical Supercapacitor Performance

Chunhui Wu, Zifan Pei, Menglin Lv, Duchun Huang, Yuan Wang * and Shaojun Yuan *

Low-Carbon Technology & Chemical Reaction Engineering Lab, College of Chemical Engineering, Sichuan University, Chengdu 610065, China

* Correspondence: wangyuan2022@scu.edu.cn (Y.W.); ysj@scu.edu.cn (S.Y.)

Abstract: It is highly attractive to design pseudocapacitive metal oxides as anodes for supercapacitors (SCs). However, as they have poor conductivity and lack active sites, they generally exhibit an unsatisfied capacitance under high current density. Herein, polypyrrole-coated low-crystallinity Fe₂O₃ supported on carbon cloth (D-Fe₂O₃@PPy/CC) was prepared by chemical reduction and electrodeposition methods. The low-crystallinity Fe₂O₃ nanorod achieved using a NaBH₄ treatment offered more active sites and enhanced the Faradaic reaction in surface or near-surface regions. The construction of a PPy layer gave more charge storage at the Fe₂O₃/PPy interface, favoring the limitation of the volume effect derived from Na⁺ transfer in the bulk phase. Consequently, D-Fe₂O₃@PPy/CC displayed enhanced capacitance and stability. In 1 M Na₂SO₄, it showed a specific capacitance of 615 mF cm⁻² (640 F g⁻¹) at 1 mA cm⁻² and still retained 79.3% of its initial capacitance at 10 mA cm⁻² after 5000 cycles. The design of low-crystallinity metal oxides and polymer nanocomposites is expected to be widely applicable for the development of state-of-the-art electrodes, thus opening new avenues for energy storage.

Keywords: supercapacitors; anode; low-crystallinity Fe₂O₃; polypyrrole; aqueous electrolyte



Citation: Wu, C.; Pei, Z.; Lv, M.; Huang, D.; Wang, Y.; Yuan, S. Polypyrrole-Coated Low-Crystallinity Iron Oxide Grown on Carbon Cloth Enabling Enhanced Electrochemical Supercapacitor Performance. *Molecules* **2023**, *28*, 434. <https://doi.org/10.3390/molecules28010434>

Academic Editor: Chongjun Zhao

Received: 7 December 2022

Revised: 22 December 2022

Accepted: 30 December 2022

Published: 3 January 2023



Copyright: © 2023 by the authors. Licensee MDPI, Basel, Switzerland. This article is an open access article distributed under the terms and conditions of the Creative Commons Attribution (CC BY) license (<https://creativecommons.org/licenses/by/4.0/>).

1. Introduction

The energy crisis and the environmental pollution problem caused by the excessive use of fossil energy have resulted in higher demand for developing sustainable energy around the world [1,2]. It is highly attractive to develop electrochemical energy storage devices by utilizing renewable energy sources (e.g., tidal, wind, and solar energy) [3,4]. Among the diverse energy storage devices, supercapacitors (SCs) have attracted considerable attention due to their high power density (1–10 kW kg⁻¹), fast charge/discharge rate, safety, and long lifespan (>100,000 cycles) [5,6]. Electric double-layer capacitor (EDLC) materials are widely employed in SCs because of their high electrical conductivity, large specific surface area, and low cost [7]. However, the energy storage mechanism of EDLCs occurs at the surface of the electrode, which is responsible for the EDLCs' poor capacity compared with batteries [8,9]. In addition, according to the equation $E = 1/2CV^2$, constructing asymmetric supercapacitor devices (ASCs) can widen the operating voltage window and enhance the energy density [10]. However, the capacitance of ASCs is mainly limited by the inferior capacitance of negative materials.

Metal oxides, such as the pseudocapacitor materials (e.g., Co₃O₄, MnO₂, and Bi₂O₃), can offer a higher specific capacitances than EDLC materials because of the charge storage mechanism of surface/near-surface redox reactions [11–15]. Among these metal oxides, Fe₂O₃ is one of the most interesting negative materials due to its low cost, environmental benignity, wide operating voltage window (0 to −0.1 V vs. Ag/AgCl), and so on [16,17]. However, it has usually exhibited an insufficient ionic diffusion rate, inferior electronic conductivity, and a volume effect, leading to poor specific capacitance and stability [18,19].

Generally, designing nanomaterials such as nanorods [20], nanosheets [21], and quantum dots [22] can give a sufficient surface area to make good use of active materials. In addition, low-crystallinity nanomaterials are capable of achieving better electrochemical performances than their high-crystallinity counterparts due to their increased structural disorder and defects [23,24]. Xia et al. [19] fabricated a crystalline/amorphous Fe_2O_3 nanocomposite to boost the utilization of active materials and enhance the Faradaic reaction, and it delivered a capacitance of 350 mF cm^{-2} at 1 mA cm^{-2} . A defective Fe_2O_3 nanorod prepared using annealing under an inert atmosphere was reported by Wang et al. [25], and it displayed a capacitance of 381 mF cm^{-2} at 0.5 mA cm^{-2} . However, the enhancement of capacitance derived from the boosted valence state change of metal oxide usually causes irreversible conversion in the bulk phase. Therefore, apart from the design of the nanostructure, it is imperative to develop strategies that can transform “bulk” redox reactions into “surface/near-surface” levels of redox reaction, which can simultaneously achieve the capacitance and electrochemical stability.

The construction of nanocomposites by introducing advanced carbon materials or conductive polymers not only favors the electron transfer of electrodes but also hinders the volume effect to improve the cycling stability [26,27]. Polypyrrole (PPy), a heterocyclic conjugate conductive polymer, has attracted considerable attention in energy storage devices [28,29]. Yang et al. [30] prepared a flexible PPy@ Fe_2O_3 @stainless steel yarn composite electrode and enhanced the capacitance compared with the Fe_2O_3 @stainless steel yarn. Obaidat et al. [31] reposted a PPy-assisted Ag-doping strategy to improve the electrochemical performance of $\text{Co}(\text{OH})_2$, and the cycling stability was obviously improved after introducing PPy. Compared with the introduction of PPy by chemical oxidation, the electrodeposition strategy is considered to be a promising route for boosting energy storage. PPy prepared using electrochemical deposition methods was reported, and it possessed a molecular ordering formation assisted by an electric field [32]. By depositing a polymer on the surface of electrode to form the core-shell nanostructure, the formative interface between the polymer and the metal oxide can serve as the reservoir to achieve energy storage [33]. Moreover, this interface can efficiently limit ion transfer in the bulk phase, thus hindering the volume effect and further contributing to the electrochemical stability [33]. A low-crystallinity metal oxide with high disorder can usually possess a high charge storage due to the higher active area for enhancing EDLCs and Faradaic pseudocapacitance. However, they usually deliver low cycling stability. A conductive polymer coating layer can serve as the buffer layer to limit the volume expansion of active material and form an active interface to hinder the electrolyte ion transfer in the bulk phase. This could be an efficient strategy to boost the cycling stability. Therefore, we anticipate the construction of low-crystallinity Fe_2O_3 coated with a PPy layer, which can simultaneously boost capacitance and electrochemical stability.

In this work, we first constructed low-crystallinity Fe_2O_3 nanorod arrays on carbon cloth (D- $\text{Fe}_2\text{O}_3/\text{CC}$) using a simple chemical reduction reaction to enlarge the interface of the electrolyte and electrode. Then, PPy was deposited on the surface of low-crystallinity Fe_2O_3 using an electrochemical deposition method to construct a metal oxide/polymer core-shell nanocomposite (D- Fe_2O_3 @PPy/CC). The NaBH_4 treatment provided a rougher surface for D- $\text{Fe}_2\text{O}_3/\text{CC}$, favoring the Faradaic reaction derived from the ion diffusion in the bulk phase. The formation of a PPy layer on the surface of D- Fe_2O_3 enhanced the charge storage on the surface or near the surface of the electrode. Compared with the pristine $\text{Fe}_2\text{O}_3/\text{CC}$ electrode with a capacitance of 114 mF cm^{-2} (123 F g^{-1}) at 1 mA cm^{-2} , this D- Fe_2O_3 @PPy/CC electrode delivered an enhanced capacitance of 615 mF cm^{-2} (640 F g^{-1}) at 1 mA cm^{-2} . Notably, the D- Fe_2O_3 @PPy/CC electrode also exhibited superior cycling stability, with an initial capacity retention of 79% at a current density of 10 mA cm^{-2} after 5000 cycles, which is higher than the initial capacity retention values of $\text{Fe}_2\text{O}_3/\text{CC}$ (42%) and D- $\text{Fe}_2\text{O}_3/\text{CC}$ (24%) electrodes.

2. Results and Discussion

The scheme of the fabrication of D-Fe₂O₃@PPy/CC is displayed in Figure 1a. First, Fe₂O₃ nanorod arrays were prepared on carbon cloth using a simple hydrothermal reaction and then immersed in 1 M NaBH₄ to construct low-crystallinity Fe₂O₃ nanoarrays. To investigate the relationship between the reducing process and the electrochemical performance, D-Fe₂O₃/CC samples were prepared using various immersion times. After being treated with NaBH₄, the D-Fe₂O₃/CC was coated with PPy to further improve the electrochemical stability. The amount of PPy loading could easily be regulated by changing the electrodeposition time.

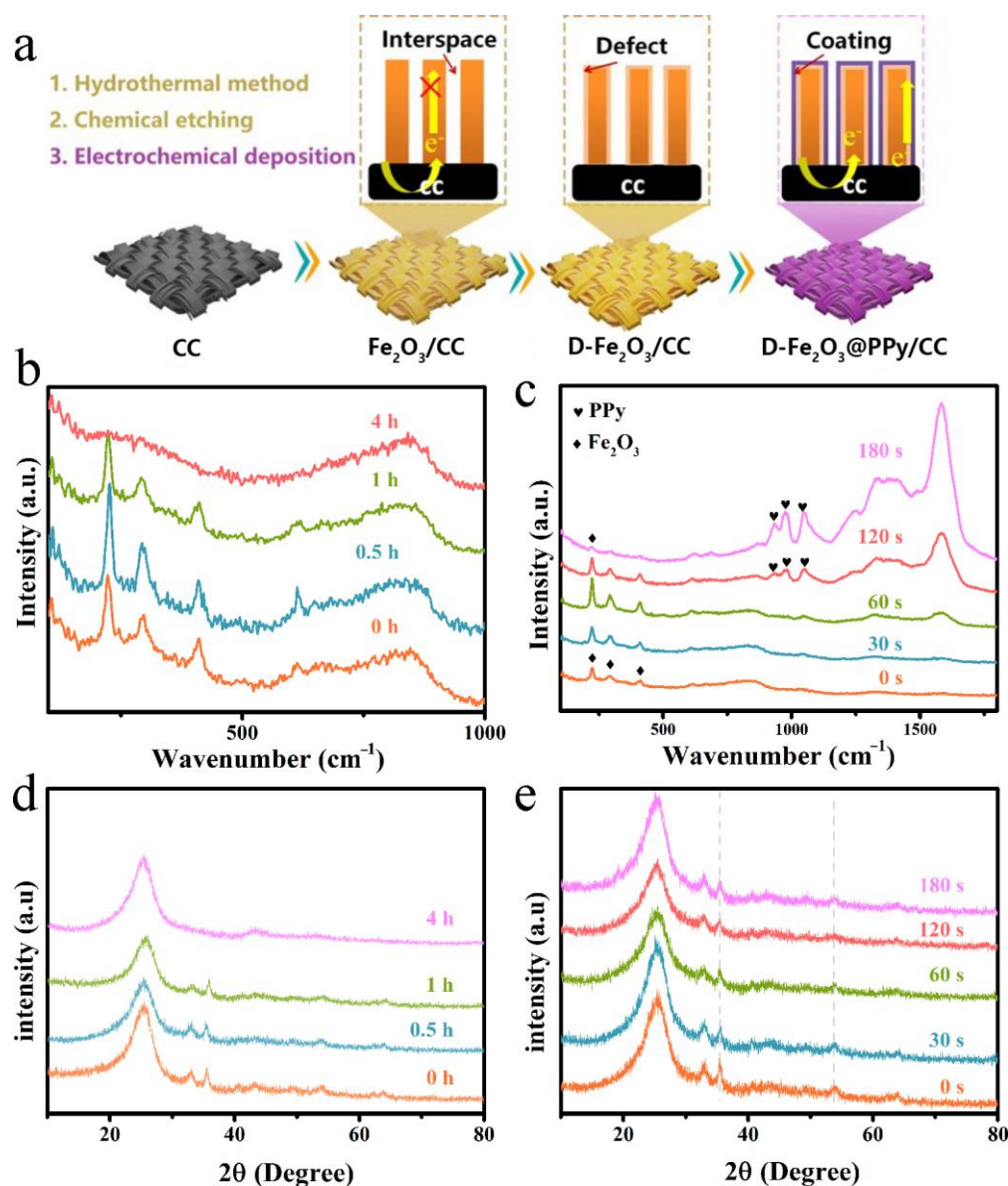


Figure 1. (a) Schematic illustration of the fabrication process of a D-Fe₂O₃@PPy/CC electrode. Raman spectra of (b) D-Fe₂O₃-xh (x = 0.5, 1, and 4) and (c) D-Fe₂O₃@PPy-ys (y = 30, 60, 120, and 180) electrodes. The corresponding XRD patterns of (d) D-Fe₂O₃-xh and (e) D-Fe₂O₃@PPy-ys electrodes.

Figure 1b displays the Raman spectra of D-Fe₂O₃/CC electrodes obtained by changing the reduction time. Clearly, three distinct peaks at 408, 291, and 223 cm⁻² are observed for the pristine Fe₂O₃, D-Fe₂O₃-0.5 h, and D-Fe₂O₃-1 h, which imply the successful preparation of Fe₂O₃ [33,34]. No obvious characteristic peak can be observed in the Raman spectrum

of D-Fe₂O₃-4 h, which indicates the breakdown of crystallinity on the Fe₂O₃ surface by the NaBH₄ treatment. The Raman spectra of D-Fe₂O₃@PPy/CC obtained by varying the electrodeposition time (Figure 1c) also show the characteristic peaks of Fe₂O₃, but decreased intensity is observed for D-Fe₂O₃@PPy-120 s and D-Fe₂O₃@PPy-180 s, which is due to the PPy coating on the surface of Fe₂O₃. Notably, the obvious characteristic peaks at 1040, 954, and 916 cm⁻¹ are observed, indicating the formation of PPy on the surface of Fe₂O₃ [33]. Similar results can be also observed in the XRD patterns of the D-Fe₂O₃/CC electrodes. As shown in Figure 1d, the characteristic peaks at 33.0°, 35.7°, 41.06°, 54.4°, and 64.3° are attributed to the (104), (110), (113), (116), and (300) planes of Fe₂O₃ (JCPDS#84-0308). The intensity of these characteristic peaks decreased by increasing the reduction time, which indicates the low crystallinity of Fe₂O₃ after the NaBH₄ treatment. The NaBH₄ treatment led to a reduction in crystal size, thus favoring Na⁺ diffusion near the surface. After being coated with PPy, no obvious change was observed (Figure 1e). This result indicates that the electrodeposition of PPy cannot influence the crystal structure of Fe₂O₃.

The surface chemistry of Fe₂O₃/CC, D-Fe₂O₃/CC, and D-Fe₂O₃@PPy/CC were investigated by XPS measurement, as shown in Figure 2. The high-resolution Fe 2p spectrum of Fe₂O₃/CC (Figure 2a) exhibits two peaks with binding energies (BEs) of 711.5 and 725.1 eV, corresponding to Fe 2p_{3/2} and Fe 2p_{1/2}, respectively. The Fe 2p_{3/2} and Fe 2p_{1/2} peaks with 13.6 eV peak separation are attributed to the typical doublet peaks of Fe³⁺, implying the existence of an Fe³⁺ species [10]. This can be further confirmed by the satellite peak of Fe 2p_{3/2} with BEs at 719.1 eV [17,35]. After the NaBH₄ treatment, the Fe 2p core-level XPS spectrum of D-Fe₂O₃/CC (Figure 2c) exhibited a negative shift compared with that of the pristine Fe₂O₃/CC, implying that the NaBH₄ treatment influences the local chemical states of Fe³⁺. This result indicates the formation of oxygen vacancy on Fe₂O₃ [25,36]. The low-crystalline and high-disorder Fe₂O₃ can provide more ion diffusion pathways, which further enhance the Faradaic reaction in the bulk phase. The high-resolution O 1s spectrum of Fe₂O₃/CC (Figure 2b) shows three peaks. The peaks with BEs at around 530.4, 531.9, and 533.2 eV are assigned to lattice oxygen, chemisorbed oxygen, and physically adsorbed oxygen, respectively [10,37]. Among them, the chemisorbed oxygen, such as O⁻, O²⁻, and O₂²⁻ on the surfaces of materials, is attributed to the adsorption oxygen on the unpaired electrons generated by the surface defects. The relative contents of these O species can be determined from the proportional areas of the corresponding peaks. After the NaBH₄ treatment, the O 1s spectrum of D-Fe₂O₃/CC (Figure 2d) showed four peaks with BEs at 529.6, 531.5, 533.1, and 535.5 eV, corresponding to the lattice oxygen, chemisorbed oxygen, physically adsorbed oxygen, and water [38,39]. As expected, the content of chemisorbed oxygen presented by D-Fe₂O₃/CC was calculated to be 36.8%, which was higher than that of pristine Fe₂O₃/CC (27.1%). This further confirmed the higher defect presentation after the chemical reduction procedure. After PPy coating, the wide-scan XPS spectrum of D-Fe₂O₃@PPy/CC (Supplementary Materials: Figure S1) exhibited the existence of N, Fe, O, C elements on the surface. The Fe 2p_{3/2} peak at 711.3 eV and the Fe 2p_{1/2} peak at 724.9 eV of D-Fe₂O₃@PPy/CC (Figure 2e) showed positive shifts compared with that of D-Fe₂O₃/CC. In addition, the high-resolution O 1s spectrum (Figure 2f) displayed two main peaks that can be deconvoluted into four peaks for 530.3, 531.7, 532.8, and 535.7 eV. The content of chemisorbed oxygen was determined to be 28%, which was due to the cover of PPy on the surface of Fe₂O₃. Figure S2 displays the high-resolution N 1s spectrum, and three deconvoluted peaks are observed at 397.7, 399.8, and 402.1 eV, which are ascribed to the Pyridinic-N, Pyrrolic-N, and nitrogen oxide, respectively [40–42]. This further indicates the successful formation of PPy on the surface of Fe₂O₃.

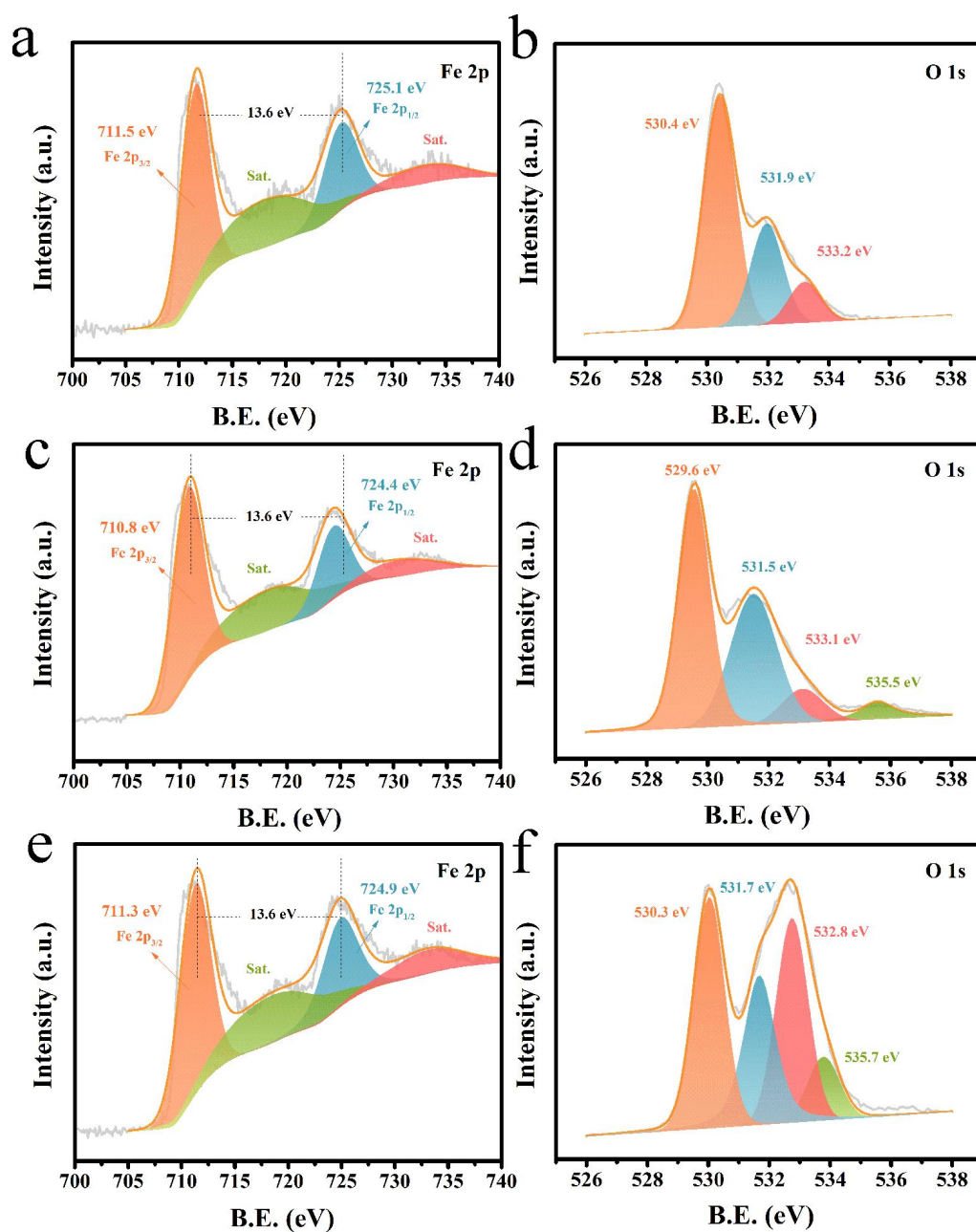


Figure 2. The XPS spectra of $\text{Fe}_2\text{O}_3/\text{CC}$ for (a) Fe 2p and (b) O 1s regions. The XPS spectra of D- $\text{Fe}_2\text{O}_3/\text{CC}$ for (c) Fe 2p and (d) O 1s regions. The XPS spectra of D- $\text{Fe}_2\text{O}_3@\text{PPy}/\text{CC}$ for (e) Fe 2p and (f) O 1s regions.

The morphology of all electrodes was investigated by SEM measurement. Clearly, the SEM image of $\text{Fe}_2\text{O}_3/\text{CC}$ (Figure 3a) displays a nanorod structure, which uniformly covers the CC fiber (Figure 3a inset). Notably, by increasing the NaBH_4 treatment time the morphology of the nanorod changed. When the reduction time was 0.5 h, some nanosheet structure between the nanorod was observed, as shown in Figure 3b. When the immersion time was more than 1 h, the SEM images of D- Fe_2O_3 -1 h and D- Fe_2O_3 -4 h (Figure 3c,d) mainly displayed nanosheet morphology. This could be ascribed to structure conversion by the NaBH_4 treatment, which provides a strong reduction reaction on the surface of Fe_2O_3 . A part of an oxygen atom is removed in the reduction reaction, giving a rougher surface for ion transfer.

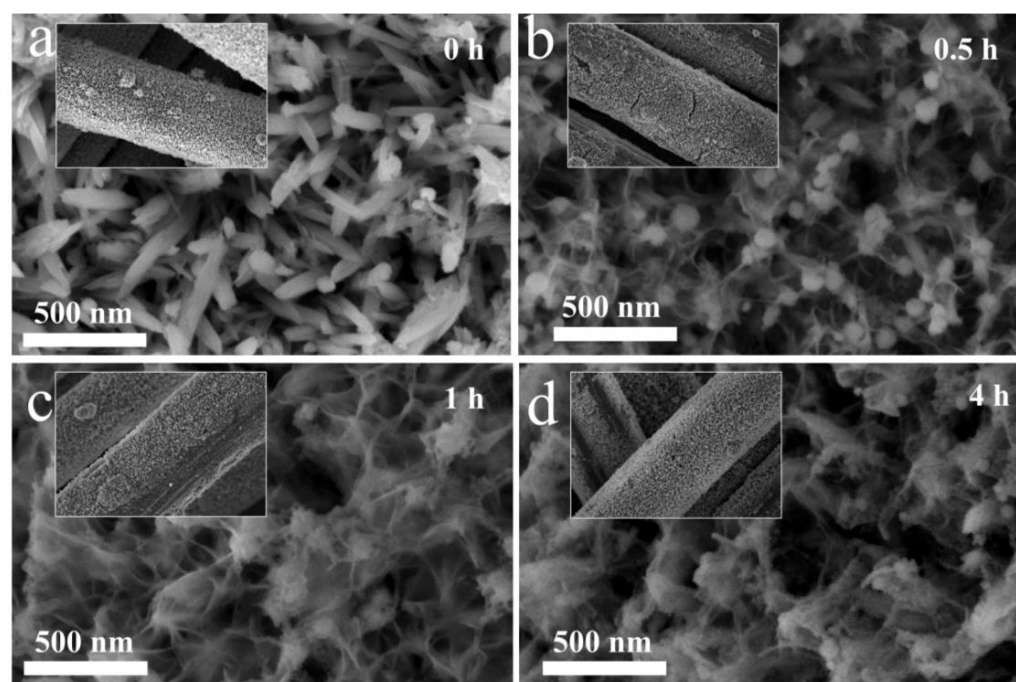


Figure 3. SEM images of D-Fe₂O₃/CC electrode prepared using different immersion times: (a) pristine Fe₂O₃, (b) D-Fe₂O₃-0.5 h, (c) D-Fe₂O₃-1 h, and (d) D-Fe₂O₃-4 h.

Figure 4 shows the SEM images of D-Fe₂O₃@PPy/CC electrodes prepared using different electrodeposition times. No obvious change could be seen when conducting PPy electrodeposition for 30 s (Figure 4a). As the electrodeposition time increased to 60 s, some nonuniform particles were embedded on the surface of electrode and the nanostructure covered the CC fiber well. When conducting PPy electrodeposition for 120 s, the nanostructure was uniformly coated with PPy (Figure 4c). However, when the electrodeposition increased to 180 s, the nanorod or nanosheet structure could not be found (Figure 4d) and the PPy aggregated on the surface of the electrode (Figure 4d inset). Excessive PPy could obstruct the ion diffusion pathway, thus hindering ion transfer and limiting the utilization of the active material. The TEM image of D-Fe₂O₃@PPy (Figure S3) shows the rough surface, which is ascribed to the result of the SEM image. In addition, the selected area electron diffraction (SAED) pattern (Figure S3 inset) shows clear diffraction rings, indicating the disordered and polycrystalline features of Fe₂O₃.

To investigate the electrochemical performances of all electrodes, a three-electrode system was used in a 1 M Na₂SO₄ aqueous electrolyte. Figure S4a–d display the CV curves of D-Fe₂O₃/CC electrodes at different scan rates. Clearly, by increasing the NaBH₄ treatment time, the area of the CV curve increased gradually. The corresponding GCD curves of D-Fe₂O₃/CC electrodes are illustrated in Figure S5a–d. The pristine Fe₂O₃, D-Fe₂O₃-0.5 h, D-Fe₂O₃-1 h, and D-Fe₂O₃-4 h electrodes delivered capacitances of 113, 701, 960, and 1220 mF cm⁻² at a current density of 1 mA cm⁻², respectively. Notably, the capacitance of Fe₂O₃/CC can be improved considerably by this chemical reduction treatment. This is ascribed to the formation of a rougher surface, which boosts the ion transfer and the utilization of the active materials. Notably, a weak charge/discharge platform at -0.6 V can be found in the GCD curves for the D-Fe₂O₃-0.5 h, D-Fe₂O₃-1 h, and D-Fe₂O₃-4 h electrodes. This implies enhanced ion transfer and Faradaic reaction in the bulk phase, which could provide additional battery-like charge storage. Figures 5a and S6a–d show the CV curves of D-Fe₂O₃@PPy/CC electrodes. All CV curves show relatively quasi-rectangular shapes, implying that they exhibited more surface Faradaic reactions. The corresponding GCD curves (Figures 5b and S7) present relatively asymmetric triangle shapes, further indicating the capacitive behavior of D-Fe₂O₃@PPy/CC electrodes. However, as the PPy electrodeposition time increased, the capacitance of the D-Fe₂O₃@PPy/CC electrode presented a

decreased capacity. This was due to the limitation of Na^+ transfer in the bulk phase of Fe_2O_3 due to the construction of the $\text{Fe}_2\text{O}_3/\text{PPy}$ interface, which could favor electrochemical stability during the charge/discharge process. The rate performance of $\text{D-Fe}_2\text{O}_3/\text{CC}$ is shown in Figure 5c. Clearly, the pristine $\text{Fe}_2\text{O}_3/\text{CC}$ only delivered capacitances of 114, 103, 89, 79, and 69 mF cm^{-2} (123, 111, 96, 85, and 74 F g^{-1}) at current densities of 1, 2, 5, 10, and 20 mA cm^{-2} , respectively. After PPy coating, the $\text{D-Fe}_2\text{O}_3@\text{PPy}/\text{CC}$ ($\text{D-Fe}_2\text{O}_3@\text{PPy-120 s}$) electrode (Figure 5d) delivered capacitances of 615, 525, 389, 298, and 208 mF cm^{-2} (640, 547, 405, 310, and 217 F g^{-1}) at 1, 2, 5, 10, and 20 mA cm^{-2} , respectively. This indicates the enhanced electrochemical performance of the Fe_2O_3 electrode using chemical reduction and PPy electrodeposition methods. In fact, the NaBH_4 treatment can provide more surface roughness for Fe_2O_3 and give ion-insertion-like charge storage in the bulk phase, which can enhance the specific capacitance but deteriorate the volume effect. The construction of an $\text{Fe}_2\text{O}_3/\text{PPy}$ interface could confine the Na^+ and limit diffusion in the bulk phase, thus providing more surface Faradaic reactions for charge storage. Table S1 lists the detailed comparisons of Fe_2O_3 -based and $\text{D-Fe}_2\text{O}_3@\text{PPy}/\text{CC}$ anodes for supercapacitors [18,19,33,34,43–49]. The results further indicate the outstanding electrochemical performance of this $\text{D-Fe}_2\text{O}_3@\text{PPy}/\text{CC}$ electrode.

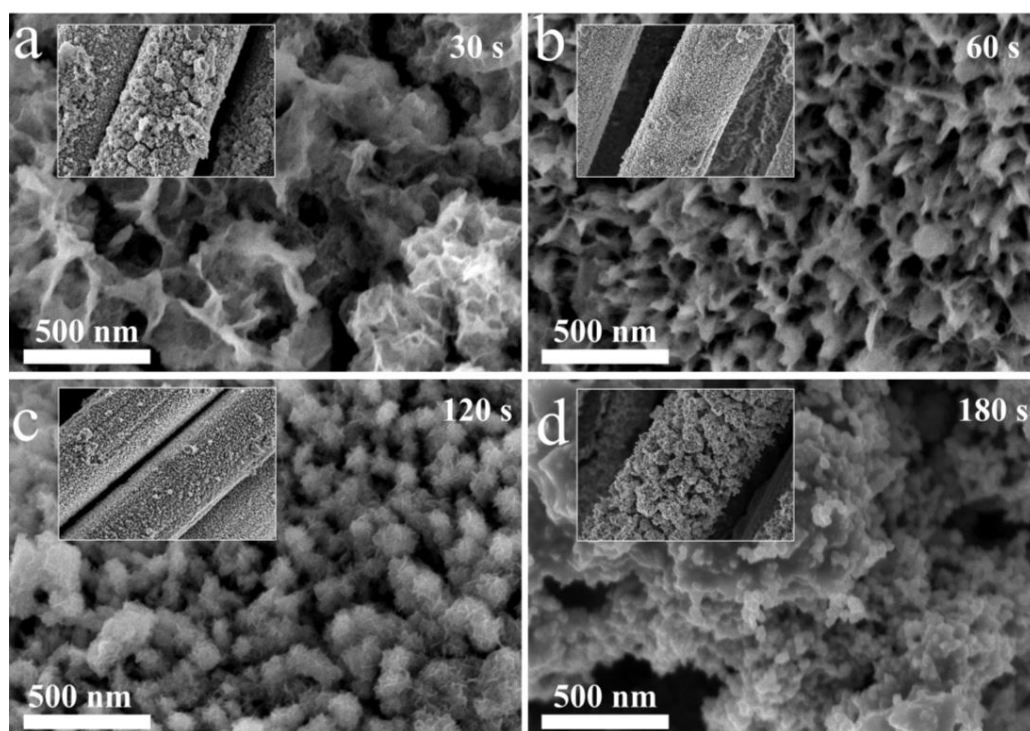


Figure 4. SEM images of $\text{D-Fe}_2\text{O}_3@\text{PPy}/\text{CC}$ electrode prepared using different electrodeposition times: (a) $\text{D-Fe}_2\text{O}_3@\text{PPy-30 s}$, (b) $\text{D-Fe}_2\text{O}_3@\text{PPy-60 s}$, (c) $\text{D-Fe}_2\text{O}_3@\text{PPy-120 s}$, and (d) $\text{D-Fe}_2\text{O}_3@\text{PPy-180 s}$.

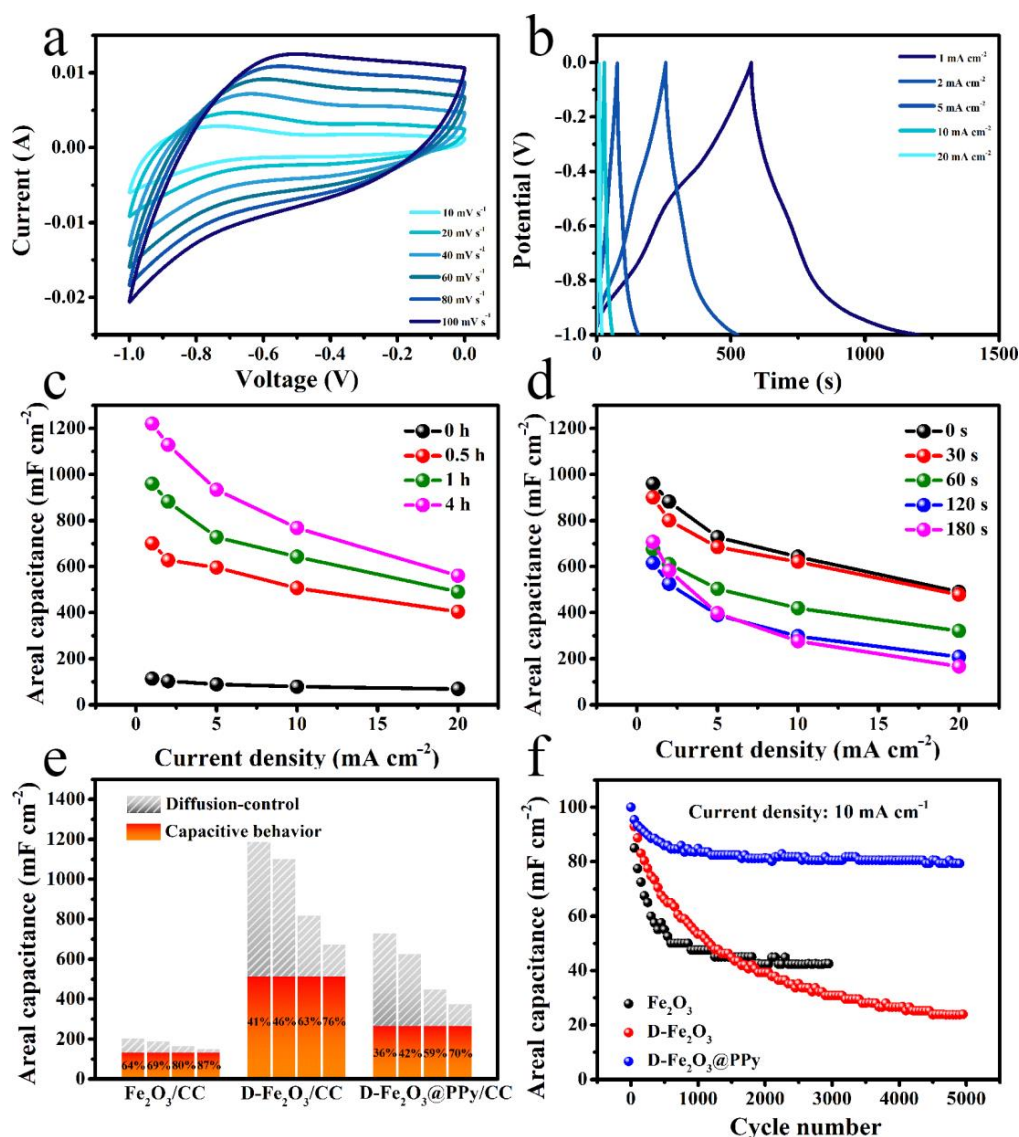


Figure 5. (a) CV curves of D-Fe₂O₃@PPy/CC (D-Fe₂O₃@PPy-120 s) at different scan rates. (b) GCD curves of D-Fe₂O₃@PPy/CC (D-Fe₂O₃@PPy-120 s) at different current densities. (c) Rate performances of D-Fe₂O₃/CC electrodes. (d) Rate performances of D-Fe₂O₃@PPy/CC electrodes. (e) Diffusion and capacitive contributions of Fe₂O₃/CC, D-Fe₂O₃/CC (D-Fe₂O₃-1 h), and D-Fe₂O₃@PPy/CC (D-Fe₂O₃@PPy-120 s) electrodes at scan rates of 10, 20, 60, 100 mV s⁻¹. (f) Long-cycling performances at current density of 10 mA cm⁻¹ for 5000 cycles.

To further investigate the charge storage mechanism, the surface capacitive behavior and diffusion-controlled contributions were divided using Dunn's method to analyze the CV data according to the equation $i(V) = k_1 v^{1/2} + k_2 v$, where $k_1 v^{1/2}$ and $k_2 v$ represent the contributions from diffusion-controlled (a slow Faradaic reaction) and surface capacitive contributions (including EDLCs and fast surface Faradaic reactions). Usually, the enlarged specific area provided by the nanoarray structure and surface roughness can offer more EDLC capacitance (ion adsorption/desorption). The active sites of the electrode surface can give more Faradaic reactions from the increased chemisorbed redox sites on the surface of electrode. These two contributions compose the surface capacitive behavior. In addition, ion insertion/deinsertion in the near-surface region offers another redox reaction from the diffusion-controlled contribution. Figure 5e compares the diffusion-controlled and capacitive contribution for the pristine Fe₂O₃/CC, D-Fe₂O₃/CC (D-Fe₂O₃-1 h), and D-Fe₂O₃@PPy/CC (D-Fe₂O₃@PPy-120 s) electrodes. Notably, the diffusion-controlled ca-

capacity gradually decreased with the increased scan rate, implying that the entry of Na^+ into the Fe_2O_3 bulk phase was limited at a high scan rate because of the electrochemical kinetic principle [50]. Owing to the “etching” process derived from the NaBH_4 treatment, Fe_2O_3 could react with NaBH_4 and generate structure defects on the surface of Fe_2O_3 , offering more active sites and ion diffusion pathways. The diffusion-controlled and capacitive behavior contributions were improved considerably for the D- $\text{Fe}_2\text{O}_3/\text{CC}$ electrode. Notably, capacitive contributions of 64%, 69%, 80%, and 87% were achieved for $\text{Fe}_2\text{O}_3/\text{CC}$ electrode at scan rates of 10, 20, 60, and 100 mV s^{-1} , respectively. After the NaBH_4 treatment, the D- $\text{Fe}_2\text{O}_3/\text{CC}$ electrode delivered decreased capacitive contributions (41%, 46%, 63%, and 76%) at different scan rates. This result confirms the enhanced ion-insertion-like charge storage. After PPy coating, the capacitive contribution further decreased, which was due to the PPy cover on the rough surface of Fe_2O_3 , thus leading to the limitation of EDLCs. Notably, the electrochemical stability was promoted considerably. As shown in Figure 5f, the D- $\text{Fe}_2\text{O}_3@\text{PPy}/\text{CC}$ electrode displayed enhanced cycling stability with a capacitance retention of 79.3% at a current density of 10 mA cm^{-2} after 5000 cycles. However, the D- $\text{Fe}_2\text{O}_3/\text{CC}$ electrode with a high specific capacitance delivered poor cycling stability, and it only retained 23.9% of its initial capacitance. The pristine $\text{Fe}_2\text{O}_3/\text{CC}$ also exhibited an unsatisfied capacitance retention of 42.5%. To further confirm the enhanced stability, the SEM images of $\text{Fe}_2\text{O}_3/\text{CC}$ and D- $\text{Fe}_2\text{O}_3@\text{PPy}/\text{CC}$ after the cycling test are displayed in Figure S8. Clearly, the nanostructure could not be maintained for the $\text{Fe}_2\text{O}_3/\text{CC}$ electrode, and the collapse of the nanostructure was observed (Figure S7a). Notably, the SEM images of the D- $\text{Fe}_2\text{O}_3@\text{PPy}/\text{CC}$ electrode show an obvious nanosheet structure (Figure S7b), and it covered the CC fiber well (Figure S8b inset).

3. Materials and Methods

3.1. Materials

Polypyrrole ($\text{C}_4\text{H}_5\text{N}$, >99%) was purchased from Aladdin Chemical Co., Ltd. (Shanghai, China). Nitric acid (HNO_3 , >68%), ethanol ($\text{C}_2\text{H}_5\text{OH}$, >99%), ferric chloride ($\text{FeCl}_3 \cdot 6\text{H}_2\text{O}$, >99%), sodium sulfate (Na_2SO_4 , >99%), sodium borohydride (NaBH_4 , >99%), and other chemical reagents were purchased from Chengdu Kelong Chemical Reagent Factory, China. The carbon cloth was purchased from Hongshan District, Wuhan Instrument Surgical Instruments (Wuhan, China). All chemical reagents were used as received without further purification.

3.2. Synthesis of $\text{Fe}_2\text{O}_3/\text{CC}$

The carbon cloth (CC) was cut into a number of $2 \times 3 \text{ cm}^2$ rectangles, immersed in concentrated HNO_3 , and heated in an oven at 110 $^\circ\text{C}$ for 2 h to attach hydroxyl on the surface of CC and remove the impurity on the surface. After the oven cooled to room temperature, the CC was washed with deionized water and ethanol for 30 min under ultrasonic conditions. Subsequently, 0.4 g of $\text{FeCl}_3 \cdot 6\text{H}_2\text{O}$ and 0.24 g of Na_2SO_4 were added to 35 mL of deionized water for dissolution. Then, the mixed solution was transferred into a 40 mL Teflon-lined stainless-steel autoclave, and a piece of CC ($2 \times 3 \text{ cm}^2$) was immersed in the above solution and treated at 120 $^\circ\text{C}$ for 6 h to obtain the FeOOH precursor nanorod on CC. The Fe_2O_3 nanorod grown on CC ($\text{Fe}_2\text{O}_3/\text{CC}$) was obtained after heating the precursor at 450 $^\circ\text{C}$ in air for 3 h at a heating rate of 2 $^\circ\text{C min}^{-1}$. The mass loading of Fe_2O_3 on CC was measured to be 0.93 mg cm^{-2} .

3.3. Synthesis of D- $\text{Fe}_2\text{O}_3/\text{CC}$

The chemical reduction process was conducted using a 1 M NaBH_4 solution. First, 1.89 g of NaBH_4 was added to 50 mL of deionized water to form a NaBH_4 solution. Pieces of $\text{Fe}_2\text{O}_3/\text{CC}$ were immersed in the NaBH_4 solution for different times (0.5, 1, and 4 h) and then washed with water several times. The NaBH_4 has strong reducibility and can serve as an “activator” to etch the crystallinity of Fe_2O_3 . By changing the immersion time, the degree of reduction could be adjusted. The obtained low-crystallinity Fe_2O_3 on CC

was named D-Fe₂O₃-xh, where x represents the 0.5, 1, and 4 h reduction times. The mass loading of D-Fe₂O₃-1 h was measured to be 0.72 mg cm⁻².

3.4. Synthesis of D-Fe₂O₃@PPy/CC

The constant-voltage electrochemical deposition of PPy on low-crystallinity Fe₂O₃ on CC was conducted in a standard three-electrode system using D-Fe₂O₃/CC, Pt foil, and Ag/AgCl as the work, counter, and reference electrode, respectively. The electrolyte was prepared by adding 0.69 mL of a pyrrole monomer and 2.45 g of NaClO₄ to 100 mL of deionized water. The mass loading of PPy can be adjusted by changing the electrodeposition time. The applied potential was set to 0.8 V with operation times of 30 s, 60 s, 120 s, and 180 s. Finally, the D-Fe₂O₃@PPy/CC electrodes were obtained after washing with deionized water and drying at 60 °C for 8 h. The obtained D-Fe₂O₃@PPy/CC electrodes with different electrodeposition times were named D-Fe₂O₃@PPy-30 s, D-Fe₂O₃@PPy-60 s, D-Fe₂O₃@PPy-120 s, and D-Fe₂O₃@PPy-180 s. The mass loading of D-Fe₂O₃@PPy-120 s was measured to be 0.96 mg cm⁻².

3.5. Material Characterization

A Raman microscope ($\lambda = 455$ nm; Thermo Fisher Scientific Inc., Waltham, MA, USA), was used to obtain the Raman dates of all samples. A Philips PW1730 X-ray diffractometer was used to collect X-ray diffraction (XRD) patterns. The X-ray photoelectron spectroscopy (XPS) spectra of all samples were collected using an X-ray photoelectron spectrometer (AXIS NOVA, Kratos, UK). The scanning electron microscopy (SEM) images were characterized by an emission scanning electron microscope (Regulus 8230 field, Hitachi, Tokyo, Japan).

3.6. Electrochemical Measurement

A CHI660E electrochemical workstation was used to evaluate the electrochemical performance, including cyclic voltammetry (CV) and galvanostatic charge–discharge (GCD). All electrodes were measured in a three-electrode system using Pt foil as the counter electrode, Ag/AgCl as the reference electrode, and 1 M Na₂SO₄ as the electrolyte. All electrochemical performances were tested at 25 °C and ambient pressure. The specific capacitance (C, mF cm⁻²) was collected by the GCD and CV data according to the equations $C = I \times \Delta t / (S \times \Delta V)$ and $C = \int IdV / (2 \times \Delta V \times v \times S)$, respectively, where I (mA), $\int IdV$, ΔV (V), Δt (s), and v (V s⁻¹) represent the discharging current, the area of the CV curve, the potential window, the discharge time, and the scan rate, respectively. S (cm²) represents the geometric area of the working electrode (in this work, $S = 0.5$ cm²).

4. Conclusions

In summary, we demonstrated polypyrrole-coated low-crystallinity Fe₂O₃ supported on carbon cloth as the self-support anode for SCs. The chemical reduction treatment offered more surface roughness for D-Fe₂O₃/CC, favoring the Faradaic reaction derived from the ion diffusion in the bulk phase. The construction of a Fe₂O₃/PPy interface further enhanced the charge storage on the surface or near the surface of the electrode, thus efficiently hindering the volume effect of Fe₂O₃ during the charge/discharge process. Compared with the pristine Fe₂O₃/CC electrode, the enlarged surface roughness and Fe₂O₃/PPy interface gave more active sites for both Faradaic reactions and ion transfer, and the capacity contributions from diffusion-controlled and capacitive behaviors were simultaneously improved. The D-Fe₂O₃@PPy/CC electrode showed a specific capacitance of 615 mF cm⁻² at 1 mA cm⁻² and still retained 79.3% of its initial capacitance at 10 mA cm⁻² after 5000 cycles.

Supplementary Materials: The following supporting information can be downloaded at <https://www.mdpi.com/article/10.3390/molecules28010434/s1>, Figure S1: Wide-scan XPS spectrum of D-Fe₂O₃@PPy/CC electrode; Figure S2: N 1s XPS spectrum of D-Fe₂O₃@PPy/CC electrode; Figure S3: TEM image of D-Fe₂O₃@PPy and the related SAED pattern; Figure S4: CV curves of D-Fe₂O₃/CC electrodes: (a) pristine Fe₂O₃, (b) D-Fe₂O₃-0.5 h, (c) D-Fe₂O₃-1 h, and (d) D-Fe₂O₃-4 h; Figure S5: GCD curves of D-Fe₂O₃/CC electrodes: (a) pristine Fe₂O₃, (b) D-Fe₂O₃-0.5 h, (c) D-Fe₂O₃-1 h, and (d) D-Fe₂O₃-4 h; Figure S6: CV curves of D-Fe₂O₃@PPy/CC electrodes: (a) D-Fe₂O₃@PPy-30 s, (b) D-Fe₂O₃@PPy-60 s, (c) D-Fe₂O₃@PPy-120 s, and (d) D-Fe₂O₃@PPy-180 s; Figure S7: GCD curves of D-Fe₂O₃@PPy/CC electrodes: (a) D-Fe₂O₃@PPy-30 s, (b) D-Fe₂O₃@PPy-60 s, (c) D-Fe₂O₃@PPy-120 s, and (d) D-Fe₂O₃@PPy-180 s; Figure S8: SEM images of (a) Fe₂O₃/CC and (b) D-Fe₂O₃@PPy/CC electrodes after long cycling test; Table S1: Electrochemical performances of Fe₂O₃-based and D-Fe₂O₃@PPy/CC anodes for supercapacitors. Citation: [18,19,33,34,43–49].

Author Contributions: Conceptualization, S.Y. and Y.W.; methodology, S.Y.; software, Y.W.; validation, S.Y., Y.W. and C.W.; formal analysis, C.W.; investigation, C.W.; resources, S.Y.; data curation, M.L.; writing—original draft preparation, C.W., M.L., Z.P., D.H. and Y.W.; writing—review and editing, Y.W. and S.Y.; visualization, Y.W.; supervision, S.Y.; project administration, S.Y.; funding acquisition, S.Y. All authors have read and agreed to the published version of the manuscript.

Funding: This research was funded by the National Natural Science Foundation of China (No. 2197812).

Institutional Review Board Statement: Not applicable.

Informed Consent Statement: Not applicable.

Data Availability Statement: The data are contained within the article.

Acknowledgments: We acknowledge Yingming Zhu from the Institute of New Energy and Low-Carbon Technology of Sichuan University for his help with SEM characterization and Panpan Li from the Shiyanjia Lab for XPS characterization (<http://www.shiyanjia.com>) accessed on 21 December 2022. We also appreciate Xiang Lin, Wen Tian, Jie Wei, and Ji Li from the Engineering Teaching Center, School of Chemical Engineering of Sichuan University, for Raman and FTIR measurements.

Conflicts of Interest: The authors declare no conflict of interest.

Sample Availability: The samples are available from the authors.

References

1. Sun, H.; Mei, L.; Liang, J.; Zhao, Z.; Lee, C.; Fei, H.; Ding, M.; Lau, J.; Li, M.; Wang, C.; et al. Three-dimensional holey-graphene/niobia composite architectures for ultrahigh-rate energy storage. *Science* **2017**, *356*, 599–604. [CrossRef] [PubMed]
2. Xiao, X.; Song, H.; Lin, S.; Zhou, Y.; Zhan, X.; Hu, Z.; Zhang, Q.; Sun, J.; Yang, B.; Li, T.; et al. Scalable salt-templated synthesis of two-dimensional transition metal oxides. *Nat. Commun.* **2016**, *7*, 11296. [CrossRef]
3. Wang, Y.; Wang, H.; Zhang, T.C.; Yuan, S.; Liang, B. N-doped porous carbon derived from rGO-Incorporated polyphenylenediamine composites for CO₂ adsorption and supercapacitors. *J. Power Sources* **2020**, *472*, 228610. [CrossRef]
4. Wang, Y.; Xiao, J.; Wang, H.; Zhang, T.C.; Yuan, S. N-doped porous carbon derived from solvent-free synthesis of cross-linked triazine polymers for simultaneously achieving CO₂ capture and supercapacitors. *Chem. Eur. J.* **2021**, *27*, 7908–7914. [CrossRef]
5. Mourad, E.; Coustan, L.; Lannelongue, P.; Zigah, D.; Mehdi, A.; Vioux, A.; Freunberger, S.A.; Favier, F.; Fontaine, O. Biredox ionic liquids with solid-like redox density in the liquid state for high-energy supercapacitors. *Nat. Mater.* **2017**, *16*, 446–453. [CrossRef]
6. Sun, B.; Xiong, P.; Maitra, U.; Langsdorf, D.; Yan, K.; Wang, C.; Janek, J.; Schröder, D.; Wang, G. Design strategies to enable the efficient use of sodium metal anodes in high-energy batteries. *Adv. Mater.* **2020**, *32*, 1903891. [CrossRef] [PubMed]
7. Wang, Y.; Xiao, J.; Wang, H.; Zhang, T.C.; Yuan, S. Binary doping of nitrogen and phosphorus into porous carbon: A novel di-functional material for enhancing CO₂ capture and super-capacitance. *J. Mater. Sci. Technol.* **2022**, *99*, 73–81. [CrossRef]
8. Zhi, J.; Zhou, M.; Zhang, Z.; Reiser, O.; Huang, F. Interstitial boron-doped mesoporous semiconductor oxides for ultratransparent energy storage. *Nat. Commun.* **2021**, *12*, 445. [CrossRef]
9. Zhu, Z.; Liu, Z.; Yin, Y.; Yuan, Y.; Meng, Y.; Jiang, T.; Peng, Q.; Wang, W.; Chen, W. Production of a hybrid capacitive storage device via hydrogen gas and carbon electrodes coupling. *Nat. Commun.* **2022**, *13*, 2805. [CrossRef]
10. Wang, Y.; Zhang, T.; Xiao, J.; Tian, X.; Yuan, S. Enhancing electrochemical performance of ultrasmall Fe₂O₃-embedded carbon nanotubes via combusting-induced high-valence dopants. *J. Mater. Sci. Technol.* **2023**, *134*, 142–150. [CrossRef]
11. Zhang, Y.; Hu, Y.; Wang, Z.; Lin, T.; Zhu, X.; Luo, B.; Hu, H.; Xing, W.; Yan, Z.; Wang, L. Lithiation-induced vacancy engineering of Co₃O₄ with improved faradic reactivity for high-performance supercapacitor. *Adv. Funct. Mater.* **2020**, *30*, 2004172. [CrossRef]

12. Mane, S.A.; Kashale, A.A.; Kamble, G.P.; Kolekar, S.S.; Dhas, S.D.; Patil, M.D.; Moholkar, A.V.; Sathe, B.R.; Ghule, A.V. Facile synthesis of flower-like Bi₂O₃ as an efficient electrode for high performance asymmetric supercapacitor. *J. Alloys Compd.* **2022**, *926*, 166722. [[CrossRef](#)]
13. Huang, Z.; Song, Y.; Feng, D.; Sun, Z.; Sun, X.; Liu, X. High mass loading MnO₂ with hierarchical nanostructures for supercapacitors. *ACS Nano* **2018**, *12*, 3557–3567. [[CrossRef](#)] [[PubMed](#)]
14. Kumar, Y.A.; Das, H.T.; Guddeti, P.R.; Nallapureddy, R.R.; Pallavolu, M.R.; Alzahmi, S.; Obaidat, I.M. Self-supported Co₃O₄@Mo-Co₃O₄ needle-like nanosheet heterostructured architectures of battery-type electrodes for high-performance asymmetric supercapacitors. *Nanomaterials* **2022**, *12*, 2330. [[CrossRef](#)] [[PubMed](#)]
15. Moniruzzaman, M.; Anil Kumar, Y.; Pallavolu, M.R.; Arbi, H.M.; Alzahmi, S.; Obaidat, I.M. Two-dimensional core-shell structure of cobalt-doped@MnO₂ nanosheets grown on nickel foam as a binder-free battery-type electrode for supercapacitor application. *Nanomaterials* **2022**, *12*, 3187. [[CrossRef](#)] [[PubMed](#)]
16. Wang, H.; Xu, Z.; Yi, H.; Wei, H.; Guo, Z.; Wang, X. One-step preparation of single-crystalline Fe₂O₃ particles/graphene composite hydrogels as high performance anode materials for supercapacitors. *Nano Energy* **2014**, *7*, 86–96. [[CrossRef](#)]
17. Zeng, Y.; Han, Y.; Zhao, Y.; Zeng, Y.; Yu, M.; Liu, Y.; Tang, H.; Tong, Y.; Lu, X. Advanced Ti-Doped Fe₂O₃@PEDOT core/shell anode for high-energy asymmetric supercapacitors. *Adv. Energy Mater.* **2015**, *5*, 1402176. [[CrossRef](#)]
18. Wang, Y.; Xiao, J.; Zhang, T.; Ouyang, L.; Yuan, S. Single-step preparation of ultrasmall iron oxide-embedded carbon nanotubes on carbon cloth with excellent superhydrophilicity and enhanced supercapacitor performance. *ACS Appl. Mater. Interfaces* **2021**, *13*, 45670–45678. [[CrossRef](#)]
19. Sun, S.; Zhai, T.; Liang, C.; Savilov, S.V.; Xia, H. Boosted crystalline/amorphous Fe₂O₃₋₅ core/shell heterostructure for flexible solid-state pseudocapacitors in large scale. *Nano Energy* **2018**, *45*, 390–397. [[CrossRef](#)]
20. Wang, Y.; Wu, C.; Wu, Z.; Cui, G.; Xie, F.; Guo, X.; Sun, X. FeP nanorod arrays on carbon cloth: A high-performance anode for sodium-ion batteries. *Chem. Commun.* **2018**, *54*, 9341–9344. [[CrossRef](#)]
21. Wang, Y.; Pan, Q.; Jia, K.; Wang, H.; Gao, J.; Xu, C.; Zhong, Y.; Alshehri, A.A.; Alzahrani, K.A.; Guo, X.; et al. Ni₂P nanosheets on carbon cloth: An efficient flexible electrode for sodium-ion batteries. *Inorg. Chem.* **2019**, *58*, 6579–6583. [[CrossRef](#)] [[PubMed](#)]
22. Zhai, T.; Sun, S.; Liu, X.; Liang, C.; Wang, G.; Xia, H. Achieving insertion-like capacity at ultrahigh rate via tunable surface pseudocapacitance. *Adv. Mater.* **2018**, *30*, 1706640. [[CrossRef](#)] [[PubMed](#)]
23. Tang, J.; Yuan, H.; Duan, Q.; Liu, Y.; Wang, Y.; Yuan, S. Phosphorus-functionalized low-crystallinity transition-metal oxide nanorod arrays grown on carbon cloth for high-performance asymmetric supercapacitors. *Colloids Surf. A* **2022**, *654*, 130189. [[CrossRef](#)]
24. Owusu, K.A.; Qu, L.; Li, J.; Wang, Z.; Zhao, K.; Yang, C.; Hercule, K.M.; Lin, C.; Shi, C.; Wei, Q.; et al. Low-crystalline iron oxide hydroxide nanoparticle anode for high-performance supercapacitors. *Nat. Commun.* **2017**, *8*, 14264. [[CrossRef](#)]
25. Lu, X.; Zeng, Y.; Yu, M.; Zhai, T.; Liang, C.; Xie, S.; Balogun, M.; Tong, Y. Oxygen-deficient hematite nanorods as high-performance and novel negative electrodes for flexible asymmetric supercapacitors. *Adv. Mater.* **2014**, *26*, 3148–3155. [[CrossRef](#)]
26. Wu, L.; Zheng, J.; Wang, L.; Xiong, X.; Shao, Y.; Wang, G.; Wang, J.; Zhong, S.; Wu, M. PPy-encapsulated SnS₂ nanosheets stabilized by defects on a TiO₂ support as a durable anode material for lithium-ion batteries. *Angew. Chem. Int. Ed.* **2019**, *58*, 811–815. [[CrossRef](#)]
27. Shimoga, G.; Palem, R.; Choi, D.; Shin, E.; Ganesh, P.; Saratale, G.; Saratale, R.; Lee, S.; Kim, S. Polypyrrole-based metal nanocomposite electrode materials for high-performance supercapacitors. *Metals* **2021**, *11*, 905. [[CrossRef](#)]
28. Yuan, L.; Yao, B.; Hu, B.; Huo, K.; Chen, W.; Zhou, J. Polypyrrole-coated paper for flexible solid-state energy storage. *Energy Environ. Sci.* **2013**, *6*, 470–476. [[CrossRef](#)]
29. Liu, J.; Zhou, W.; Lai, L.; Yang, H.; Hua Lim, S.; Zhen, Y.; Yu, T.; Shen, Z.; Lin, J. Three dimensionals α-Fe₂O₃/polypyrrole (Ppy) nanoarray as anode for micro lithium ion batteries. *Nano Energy* **2013**, *2*, 726–732. [[CrossRef](#)]
30. Zuo, W.; Zang, L.; Wang, X.; Liu, Q.; Qiu, J.; Liang, C.; Liu, X.; Yang, C. Flexible Polypyrrole@Fe₂O₃@stainless steel yarn composite electrode for symmetric thread-like supercapacitor with extended operating voltage window in Li₂SO₄-based aqueous electrolyte. *Adv. Sustain. Syst.* **2020**, *4*, 2000173. [[CrossRef](#)]
31. Arbi, H.; Yadav, A.; Anil Kumar, Y.; Moniruzzaman, M.; Alzahmi, S.; Obaidat, I. Polypyrrole-assisted Ag doping strategy to boost Co(OH)₂ nanosheets on Ni foam as a novel electrode for high-performance hybrid supercapacitors. *Nanomaterials* **2022**, *12*, 3982. [[CrossRef](#)] [[PubMed](#)]
32. Huang, Y.; Zhu, M.; Pei, Z.; Huang, Y.; Geng, H.; Zhi, C. Extremely stable polypyrrole achieved via molecular ordering for highly flexible supercapacitors. *ACS Appl. Mater. Interfaces* **2016**, *8*, 2435–2440. [[CrossRef](#)] [[PubMed](#)]
33. Wang, Y.; Du, Z.; Xiao, J.; Cen, W.; Yuan, S. Polypyrrole-encapsulated Fe₂O₃ nanotube arrays on a carbon cloth support: Achieving synergistic effect for enhanced supercapacitor performance. *Electrochim. Acta* **2021**, *386*, 138486. [[CrossRef](#)]
34. Wang, L.; Yang, H.; Liu, X.; Zeng, R.; Li, M.; Huang, Y.; Hu, X. Constructing hierarchical tectorum-like α-Fe₂O₃/PPy nanoarrays on carbon cloth for solid-state asymmetric supercapacitors. *Angew. Chem. Int. Ed.* **2017**, *56*, 1105–1110. [[CrossRef](#)] [[PubMed](#)]
35. Wang, Y.; Zhang, Y.; Zhang, T.C.; Xiang, G.; Wang, X.; Yuan, S. Removal of trace arsenite through simultaneous photocatalytic oxidation and adsorption by magnetic Fe₃O₄@PPy@TiO₂ core-shell nanoparticles. *ACS Appl. Nano Mater.* **2020**, *3*, 8495–8504. [[CrossRef](#)]
36. Wu, X.; Liu, R.; Zhao, J.; Fan, Z. Advanced carbon materials with different spatial dimensions for supercapacitors. *Nano Mater. Sci.* **2021**, *3*, 241–267. [[CrossRef](#)]

37. Liu, H.; Huo, W.; Zhang, T.C.; Ouyang, L.; Yuan, S. Photocatalytic removal of tetracycline by a Z-scheme heterojunction of bismuth oxyiodide/exfoliated g-C₃N₄: Performance, mechanism, and degradation pathway. *Mater. Today Chem.* **2022**, *23*, 100729. [[CrossRef](#)]
38. Wang, Y.; Zhang, P.; Zhang, T.C.; Xiang, G.; Wang, X.; Pehkonen, S.; Yuan, S. A magnetic γ -Fe₂O₃@PANI@TiO₂ core-shell nanocomposite for arsenic removal via a coupled visible-light-induced photocatalytic oxidation-adsorption process. *Nanoscale Adv.* **2020**, *2*, 2018–2024. [[CrossRef](#)]
39. Wang, Y.; Liu, X.; Chen, Q.; Zhang, T.C.; Ouyang, L.; Yuan, S. Simultaneous photocatalytic oxidation and adsorption for efficient As(III) removal by magnetic BiOI/ γ -Fe₂O₃ core-shell nanoparticles. *Mater. Today Chem.* **2022**, *24*, 100823. [[CrossRef](#)]
40. Ji, W.; Xiong, Y.; Wang, Y.; Zhang, T.C.; Yuan, S. Multilayered TNAs/SnO₂/PPy/ β -PbO₂ anode achieving boosted electrocatalytic oxidation of As(III). *J. Hazard. Mater.* **2022**, *430*, 128449. [[CrossRef](#)]
41. Xiao, J.; Wang, Y.; Zhang, T.C.; Yuan, S. N,S-containing polycondensate-derived porous carbon materials for superior CO₂ adsorption and supercapacitor. *Appl. Surf. Sci.* **2021**, *562*, 150128. [[CrossRef](#)]
42. Xiao, J.; Wang, Y.; Zhang, T.C.; Ouyang, L.; Yuan, S. Phytic acid-induced self-assembled chitosan gel-derived N, P-co-doped porous carbon for high-performance CO₂ capture and supercapacitor. *J. Power Sources* **2022**, *517*, 230727. [[CrossRef](#)]
43. Sui, S.; Sha, J.; Deng, X.; Zhu, S.; Ma, L.; He, C.; Liu, E.; He, F.; Shi, C.; Zhao, N. Boosting the charge transfer efficiency of metal oxides/carbon nanotubes composites through interfaces control. *J. Power Sources* **2021**, *489*, 229501. [[CrossRef](#)]
44. Cai, D.; Du, J.; Zhu, C.; Cao, Q.; Huang, L.; Wu, J.; Zhou, D.; Xia, Q.; Chen, T.; Guan, C.; et al. Iron oxide nanoneedles anchored on N-doped carbon nanoarrays as an electrode for high-performance hybrid supercapacitor. *ACS Appl. Energy Mater.* **2020**, *3*, 12162–12171. [[CrossRef](#)]
45. Saravanakumar, B.; Ko, T.; Kim, B. Rational design of binder-free ZnCo₂O₄ and Fe₂O₃ decorated porous 3D Ni as high-performance electrodes for asymmetric supercapacitor. *Ceram. Int.* **2018**, *44*, 10635–10645. [[CrossRef](#)]
46. Liang, H.; Xia, C.; Emwas, A.; Anjum, D.; Miao, X.; Alshareef, H. Phosphine plasma activation of α -Fe₂O₃ for high energy asymmetric supercapacitors. *Nano Energy* **2018**, *49*, 155–162. [[CrossRef](#)]
47. Sun, J.; Huang, Y.; Fu, C.; Huang, Y.; Zhu, M.; Tao, X.; Zhi, C.; Hu, H. A high performance fiber-shaped PEDOT@MnO₂/C@Fe₃O₄ asymmetric supercapacitor for wearable electronics. *J. Mater. Chem. A* **2016**, *4*, 14877–14883. [[CrossRef](#)]
48. Lu, X.; Chen, X.; Zhou, W.; Tong, Y.; Li, G. α -Fe₂O₃@PANI Core-shell nanowire arrays as negative electrodes for asymmetric supercapacitors. *ACS Appl. Mater. Interfaces* **2015**, *7*, 14843–14850. [[CrossRef](#)]
49. Yang, P.; Ding, Y.; Lin, Z.; Chen, Z.; Li, Y.; Qiang, P.; Ebrahimi, M.; Mai, W.; Wong, C.; Wang, Z. Low-cost high-performance solid-state asymmetric supercapacitors based on MnO₂ nanowires and Fe₂O₃ nanotubes. *Nano Lett.* **2014**, *14*, 731–736. [[CrossRef](#)]
50. Shao, Y.; El-Kady, M.F.; Sun, J.; Li, Y.; Zhang, Q.; Zhu, M.; Wang, H.; Dunn, B.; Kaner, R.B. Design and mechanisms of asymmetric supercapacitors. *Chem. Rev.* **2018**, *118*, 9233–9280. [[CrossRef](#)]

Disclaimer/Publisher's Note: The statements, opinions and data contained in all publications are solely those of the individual author(s) and contributor(s) and not of MDPI and/or the editor(s). MDPI and/or the editor(s) disclaim responsibility for any injury to people or property resulting from any ideas, methods, instructions or products referred to in the content.